CHEMISTRY OF MATERIALS

pubs.acs.org/cm

Article

From Layered Antiferromagnet to 3D Ferromagnet: LiMnBi-to-MnBi Magneto-Structural Transformation

Volodymyr Gvozdetskyi, Khusboo Rana, Raquel A. Ribeiro, Aishwarya Mantravadi, Adedoyin N. Adeyemi, Renhai Wang, Huafeng Dong, Kai-Ming Ho, Yuji Furukawa, Paul C. Canfield, and Julia V. Zaikina*

Cite This: *Chem. Mater.* 2023, 35, 3236−3248

Read Online

ACCESS | Metrics & More | Article Recommendations | Supporting Information

ABSTRACT: The intermetallic compound LiMnBi was synthesized by the two-step solid-state reaction from the elements. A synthesis temperature of 850 K was selected based on in situ high-temperature powder X-ray diffraction data. LiMnBi crystalizes in the layered-like PbClF structure type (a = 4.3131(7) Å, c = 7.096(1) Å at 100 K, $P4/nmm$ space group, Z = 2). The LiMnBi structure is built of alternating [MnBi] and Li layers, as determined from single-crystal X-ray diffraction data. Magnetic property measurements and solid-state ^{7}Li nuclear magnetic resonance data collected for polycrystalline LiMnBi samples indicate the long-range antiferromagnetic ordering of the Mn sublattice at ∼340 K, with no superconductivity detected down to 5 K. LiMnBi is air- and water-sensitive. Under aerobic conditions, Li can be extracted from the LiMnBi structure to form Li_2O/LiOH and MnBi (NiAs structure type, $P6_3/mmc$). The obtained MnBi polymorph was previously reported to be one of the strongest rare-earth-free ferromagnets, yet its bulk synthesis in powder form is cumbersome. The proposed magneto-structural transformation from ternary LiMnBi to ferromagnetic MnBi involves condensation of the $MnBi_4$ tetrahedra upon Li deintercalation and is exclusive to LiMnBi. In contrast, ferromagnetic MnBi cannot be obtained from either isostructural NaMnBi and KMnBi or from the structurally related $CaMn_2Bi_2$. Such a distinctive transformation in the case of LiMnBi is presumed to be due to its fitting reactivity to yield MnBi and a favorable interlayer distance between [MnBi] layers, while the interlayer distance in NaMnBi and KMnBi structural analogues is unfavorably long. The studies of delithiation from layered-like LiMnBi under different chemical environments indicate that the yield of MnBi depends on the type of solvent used and the kinetics of the reaction. A slow rate and mild reaction media lead to a high fraction of the MnBi product. The saturation magnetization of the "as-prepared" MnBi is ∼50% of the expected value of 81.3 emu/g. Overall, this study adds a missing member to the family of ternary pnictides and illustrates how soft-chemistry methods can be used to obtain "difficult-to-synthesize" compounds.

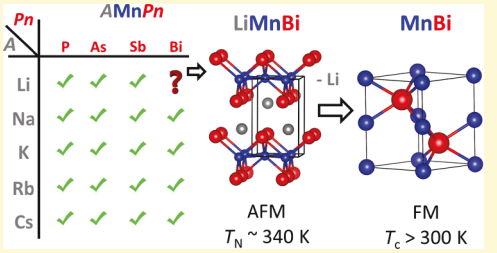

INTRODUCTION

Crystal structure and magnetic properties of equiatomic alkali metal manganese pnictides $AMnPn$ (A = alkali metal, Li−Cs; Pn = pnictogen, group 15 element) were systematically studied in the 1980s−2000s.[1−4] $AMnPn$ compounds have a layered structure (tetragonal $P4/nmm$ space group) featuring edge-sharing tetrahedra $MnPn_4$ alternating with alkali metal layers. Interest in layered compounds with a similar structure was sparked by the discovery of superconductivity in LaFePO ($P4/nmm$, T_c = 5 K) in 2006,[5] which laid the foundation for novel iron-based superconductors.[6−11] In the following decades, superconductivity with T_c ∼ 20−60 K was identified in several families of iron-based superconductors, such as 1111-, 122-, 111-, and 11-types, represented with ZrCuSiAs ($P4/nmm$), $ThCr_2Si_2$ ($I4/mmm$), PbClF ($P4/nmm$), and PbO ($P4/nmm$) structure types, respectively.[6−11] The structural phase transition from the tetragonal to orthorhombic symmetry, accompanied by commensurate antiferromagnetic ordering upon cooling, is common for the compounds in these families. Introducing electrons/holes via aliovalent chemical substitution or high pressure can suppress low-temperature phase transition and induce superconductivity in the parent layered compounds.[11−14] On the contrary, the newly identified 1144 family, with the $CaKFe_4As_4$ representative, features an ordered arrangement of monovalent and divalent cations, lacks an orthorhombic distortion, and exhibits inherent superconductivity.[15,16]

Another interesting aspect of layered compounds is that their structure is prone to deintercalation. Hence, these layered compounds can yield new metastable compounds via cation deintercalation from the parent layered structure followed by

Received: January 20, 2023
Revised: March 22, 2023
Published: April 6, 2023

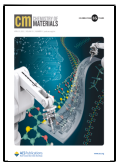

condensation of the anionic layers. For example, $NaFe_2As_2$ can be prepared by oxidative elimination of Na from NaFeAs,[17−19] metastable CoS and CoSe are the products of complete deintercalation of K^+ from KCo_2S_2 and KCo_2Se_2,[20] and $K_{1-x}Ni_2Se_2$ and $K_{1-y}Ni_{2-z}Se_2$ are obtained upon partial deintercalation of K^+ from KNi_2Se_2.[21] The complete or partial deintercalation oftentimes leads to alteration in the magnetic and other properties of the deintercalated compounds compared to their parent counterparts.

Magnetic structures were experimentally determined for most of the *A*Mn*Pn* compounds using neutron diffraction.[2−4] These structures exhibit antiferromagnetic ordering of Mn spins with a Neel temperature around room temperature, and no superconductivity down to 2 K was reported. The Mn spins align antiparallel within each [Mn*Pn*] layer in *A*Mn*Pn*. The coupling between the adjacent layers is either parallel resulting in the same magnetic unit cell as the crystallographic one or antiparallel leading to the doubling of the *c*-parameter in the magnetic unit cell compared to the nuclear cell.[2−4] Out of the 20 possible *A*Mn*Pn* compounds (*A* = Li, Na, K, Rb, and Cs; *Pn* = P, As, Sb, and Bi), only LiMnBi is "overlooked", e.g., no synthesis, structure, or properties are reported for LiMnBi.[22] An adaptive genetic algorithm (AGA), which was previously shown to successfully predict structures and stability of new compounds,[23−26] has hinted at the stability of the LiMnBi phase (*P*4/*nmm* space group). Encouraged by this, we studied the Li−Mn−Bi system and experimentally confirmed the existence of the LiMnBi compound. Here, we report on LiMnBi synthesis, structure, thermal stability, and magnetic properties. We have also found that unlike Na, K, or Ca analogues, LiMnBi transforms into strong ferromagnet MnBi upon delithiation. The results of the controlled LiMnBi decomposition yielding MnBi under different chemical environments are discussed.

EXPERIMENTAL SECTION

Synthesis of LiMnBi. Starting materials for synthesis were lithium granules (Alfa Aesar, 99%), manganese powder (Alfa Aesar, 99.95%), and bismuth lumps (Alfa Aesar, 99.9%). All manipulations of reagents and samples were carried out under an inert argon atmosphere ($p(O_2)$ < 1 ppm, $p(H_2O)$ < 1 ppm) in a glovebox. Bismuth powders were prepared by ball-milling bismuth lumps for 12 min in the ambient atmosphere using a 5 mL tungsten carbide lined grinding vial set and a high-energy ball-mill SPEX 8000 M MIXER/MILL. Afterward, in glovebox lithium granules and powders of manganese and bismuth were weighted in the desired molar ratio (Li:Mn:Bi = (1.05−1.11):(1.00−1.07):1, total mass m = 0.3 g) and loaded into a tantalum container that was sealed by arc-welding. The sealed tantalum ampoules were placed into a silica reactor that was evacuated to 4×10^{-5} bar. The reactor was further heated from room temperature to 850 K at a rate of 1.9 K/min, held at that temperature for 8 h, and rapidly quenched into cold water. Afterward, tantalum ampoules were opened, and samples were reground and reheated following the same heating profile. The nearly phase-pure sample of LiMnBi (∼2 wt % Bi impurity) was obtained using the Li:Mn:Bi =1.1:1.04:1 molar ratio and the heating procedure described above. The LiMnBi compound was found to be air and moisture sensitive and was stored in a glovebox.

To obtain crystals suitable for a single-crystal X-ray diffraction a heating profile with a slow cooling step was employed. Elemental precursors were heated from room temperature to 973 K at a rate of 1.5 K/min, held at that temperature for 8 h, slowly cooled to 453 K at a rate of 0.05 K/min, and cooled to room temperature by switching the furnace off. Thin, plate-shaped single crystals (approx. dimensions $0.04 \times 0.02 \times 0.005$ mm) of LiMnBi were mechanically separated for further analysis.

Controlled LiMnBi Decomposition. Controlled decomposition of LiMnBi was carried out in air, in deionized water, absolute ethanol (200 proof, 99.5%, Fisher), acetonitrile (ACS certified, 99.9%, Fisher), ethylenediamine (99.9%, Alfa Aesar), pyridine (99.5%, Alfa Aesar), DMF (dimethylformamide, 99.9%, Alfa Aesar), DMSO (dimethylsulfoxide, 99.9%, Fisher), 12-crown-4 ether (Alfa Aesar, 98%), and by leaving a sample in a glovebox with $p(O_2)$ < 1 ppm, $p(H_2O)$ < 1 ppm. All the reactions involving solvent were carried out under an inert Ar atmosphere (Schlenk line) using 25 mL flasks. Ethylenediamine was additionally purified in a solvent system, and the rest of the solvents were used as received. Approximately, 20 mg of the LiMnBi sample and 2 mL of solvent were used for each test. LiMnBi reacted rapidly with water, acetonitrile, and ethylenediamine (within a few minutes after adding solvent). Other reactions were carried out for the duration of 1 day at room temperature, except 12-crown-4 ether (reaction was carried at 348 K for 3 days). After the reactions were completed, most of the solvent was removed with a syringe, and the precipitate was dried in a vacuum oven. Oxidation of LiMnBi in a glovebox was monitored for 3 months at room temperature and for 2 months at elevated temperatures where the sample in a Petri dish was heated on a hot plate.

Laboratory Powder X-ray Diffraction. The purity of polycrystalline samples was checked by means of a Rigaku MiniFlex 600 powder diffractometer with Cu $K\alpha$ radiation (λ = 1.540593 Å) and a Ni-K_β filter. Data were collected on a holder for air-sensitive samples at room temperature. The data for air-sensitive samples were collected immediately after a sample (loaded into an air-sensitive holder) was taken out of an argon-filled glovebox to limit the time a sample is air-exposed to no longer than 10 min. Phase analysis was performed using the PDF-2 database incorporated into PDXL program software.[27] During controlled oxidation of samples in air, the corresponding powder diffractograms were collected in ∼10 min time intervals using an open zero-background plate holder.

Single-Crystal X-ray Diffraction. Single-crystal data were collected by means of a Bruker D8 VENTURE diffractometer (Photon CMOS detector, Mo-IμS microsource, and Oxford Cryosystem 800 low-temperature device) at 100 K. Crystals were immersed into viscous cryoprotectant Parabar (Paratone) oil and cooled with the stream of liquid nitrogen during data collection. Data integration, absorption correction, and unit cell determination was performed by APEX 3 software.[28] The starting atomic parameters were obtained by direct methods with SHELXS-2017.[29] Subsequently, the structure was refined using SHELXL-2017[29] (full-matrix least-squares on F_o^2). Analysis of the diffraction data revealed a tetragonal symmetry (a = 4.3131(7) Å, c = 7.096(1) Å). The systematic absences and the E-value statistics indicated two possible centrosymmetric space groups *P*4/*n* and *P*4/*nmm*. Both structure solutions imply Bi atoms occupying the 2*c* site, Mn − 2*a* site, and Li − 2*c* site; therefore, a higher symmetry space group *P*4/*nmm* has been considered. The relatively poor crystal quality leads to the ∼3.5 eÅ^3 peaks on the residual Fourier electron density map. Most of these peaks are next to the Bi site, while no residual electron density is present near the 2*b* site, consistent with PbClF, but not the LaOF structure type for LiMnBi. Moreover, refinement with Li in the 2*b* site is unstable and leads to shifting of Li to the 2*c* site. Details of the data collection and refinement are listed in Table S1, and atomic coordinates and ADPs are given in Table S2. The crystal structure was visualized using the program VESTA 3.[30] Further details of the crystal structure investigations may be obtained from the joint CCDC/FIZ Karlsruhe online deposition service: https://www.ccdc.cam.ac.uk/structures/ by quoting the deposition number CSD-2237201.

In Situ Synchrotron Powder X-ray Diffraction. High-temperature synchrotron powder X-ray diffraction (HT-PXRD) data were collected at the beamline 17-BM (APS ANL) with an average wavelength λ = 0.24158 Å. A powdered sample of LiMnBi was filled in 0.7 mm outer diameter thick-wall (0.1 mm) silica capillaries and sealed under vacuum. The capillary was mounted into a secondary shield capillary (0.9 mm inner diameter, 1.1. mm outer diameter) located on a sample stage equipped with two resistive microheaters

https://doi.org/10.1021/acs.chemmater.3c00140
Chem. Mater. 2023, 35, 3236−3248

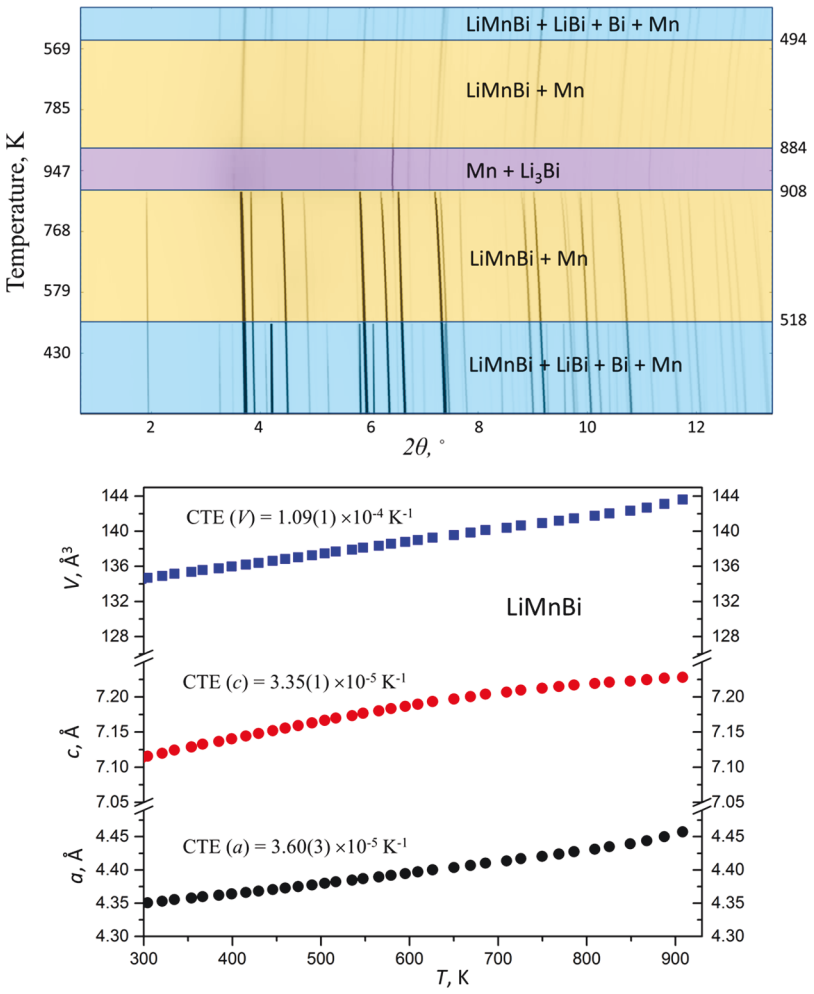

Figure 1. High-temperature in situ PXRD patterns (top), showing the transformation of a powdered sample of LiMnBi (contains LiBi, Bi, and Mn impurities and a trace amount of MnBi) sealed into an evacuated silica capillary. The "waterfall" plot shows the evolution of PXRD patterns with the temperature changing from room temperature up to 947 K. The temperature regions with distinct phase contributions are highlighted in different colors. The temperature dependence of the unit cell parameters and unit cell volume of the LiMnBi compound is shown (bottom).

and a thermocouple set as close as possible to the measurement area. Further details of the experimental setup can be found elsewhere.[31] Data were collected upon heating and cooling in the temperature range 298 K → 947 K → 298 K with variable heating and cooling rates ∼ 10−20 K·min^{-1}.

Diffraction patterns were analyzed by the Rietveld refinement method using the GSAS II software package.[32] The profile parameters, background parameters, zero correction, and cell parameters were refined first. The background was fitted using the 10-order Chebyschev polynomial function, and a pseudo-Voigt function was applied to generate the profile shape. The LiMnBi structure model determined from the single-crystal X-ray diffraction (SC-XRD) was refined via the Rietveld method using synchrotron PXRD data obtained at 17-BM at the Advanced Photon Source at Argonne National Laboratory (APS ANL). This resulted in a good fit of experimental data, R_B = 8% (Table S3, Figure S1).

^{7}Li Solid-State Nuclear Magnetic Resonance. ^{7}Li (nuclear spin I = 3/2, gyromagnetic ratio $\gamma_N/2\pi$ = 16.5471 MHz/T) nuclear magnetic resonance (NMR) measurements in the temperature range 8−469 K were carried out by using a laboratory-built phase coherent spin-echo pulsed NMR spectrometer on the polycrystalline samples enclosed in a vacuumed quartz tube. Under a fixed external magnetic field (H) of 7.4089 T, ^{7}Li-NMR spectra were taken either by measuring the spin-echo intensity while sweeping the frequency or by summing over Fourier transforms of the spin-echo signals. The ^{7}Li spin−lattice relaxation rates ($1/T_1$) were measured by the conventional single saturation pulse method. The $1/T_1$ value at each temperature was extracted using the stretched exponential fit for I = 3/2 nuclei, $1 - \frac{m(t)}{m(\infty)} = 0.9e^{-\left(\frac{6t}{T_1}\right)^{\beta}} + 0.1\, e^{-\left(\frac{t}{T_1}\right)^{\beta}}$ where $m(t)$ is the spin-echo intensity at time (t), and β is the stretching exponent. Here, β = 1 in the presence of a single value T_1, whereas β < 1 when a distribution of T_1 is present. The β values were found to be nearly constant with an average of around 0.65.

Magnetic Property Measurements. Magnetic measurements were performed on polycrystalline samples (m = 30−50 mg), which were loaded under an inert atmosphere into an EPR silica tube that was further flame-sealed under vacuum. The data were collected using a Quantum Design MPMS XL and MPMS3 SQUID magnetometer. Temperature-dependent DC magnetization measurements were carried out in an applied field of 50, 1000, 2000, 3000, 10,000, 20,000, and 40,000 Oe in the 5−375 K range. Field-dependent measurements were carried out at 2, 5, and 300 K.

Scanning Electron Microscopy and Energy-Dispersive X-ray Spectroscopy. The quantitative elemental analysis was performed with energy-dispersive X-ray spectroscopy (EDXS) using an FEI Quanta-250 field-emission scanning electron microscope, equipped with an Oxford X-Max 80 detector and an Oxford Aztec energy-dispersive X-ray analysis system. A powdered sample of delithiated LiMnBi was mounted on an aluminum stub using a double-sided carbon tape. Samples were oriented perpendicular to the beam and analyzed using a 10 kV accelerating voltage and an accumulation time

https://doi.org/10.1021/acs.chemmater.3c00140
Chem. Mater. 2023, 35, 3236−3248

of 60 s for the collection of back-scattered electron (BSE) and secondary electron (SE) images.

Computational Details. First principles calculations were carried out based on density functional theory (DFT) using VASP codes.[33,34] The projected augmented wave (PAW) method[35,36] was used to describe the electron-ion interaction, and the generalized gradient approximation (GGA) in the Perdew–Burke–Ernzerhof (PBE) form[37] was employed for the exchange-correlation energy functional. A plane-wave basis with a kinetic energy cutoff of 520 eV was used to expand the electronic wave functions, and the convergence criterion for the total energy was set to 10^{-5} eV. Monkhorst–Pack's sampling scheme[38] was adopted for Brillouin zone sampling with a *k*-point grid of $2\pi \times 0.033$ Å^{-1}, and the lattice vectors (both the unit cell shape and size) and atomic coordinates are fully relaxed until the force on each atom is less than 0.01 eV/Å.

To characterize the energetic stability of the structures, the formation energy with respect to the elemental ground-state bulk phases of the constituent elements (denoted as $E_{\text{formation}}$) is calculated.

For any given structure $Li_mMn_nBi_p$, $E_{\text{formation}}$ is defined as:

$$E_{\text{formation}} = \frac{E(Li_mMn_nBi_p) - mE(Li) - nE(Mn) - pE(Bi)}{m + n + p}$$

where $E(Li_mMn_nBi_p)$ is the total energy of the $Li_mMn_nBi_p$ compound. E(Li), E(Mn), and E(Bi) are the per-atom energy of the ground state of Li, Mn, and Bi crystals, respectively.

RESULTS AND DISCUSSION

Synthesis and Thermal Stability by In Situ HT-PXRD. Structure search using the adaptive genetic algorithm (AGA)[23−26] suggests that LiMnBi (*P*4/*nmm*) is stable with respect to elemental Li, Mn, and Bi, as evidenced by the negative formation energy, $E_{\text{formation}}$ = −0.130 eV/atom. SC-XRD data confirm that LiMnBi crystallizes with the PbClF structure type (*P*4/*nmm*) (Tables S1−S3). The synthesis of a nearly phase-pure sample was achieved via two-step annealing with intermediate grinding of the powder. In the first step, heat treatment of elemental precursors at 850 K resulted in the ternary LiMnBi phase together with binary compounds Li_3Bi, MnBi, LiBi, and unreacted Bi and Mn (Figure S2). Regrinding samples and reannealing at 850 K improved the yield of LiMnBi to ∼98 wt % (Figures S2 and S3).

To determine the optimized annealing temperature, we used in situ HT-PXRD data of the sample containing LiMnBi as the main phase together with Bi, LiBi, and Mn as impurities (Figure 1). Above 518 K, only LiMnBi with traces of elemental Mn are present while Bi and LiBi are molten (m.p. of Bi is 544 K,.m.p. of LiBi is 688 K, and m.p. of a eutectic between Bi and LiBi is 516 K). With the temperature increasing above 908 K, the ternary phase decomposes: 3LiMnBi → Li_3Bi + 2Mn + Bi. Upon cooling below 844 K, LiMnBi recrystallizes; however, the corresponding PXRD patterns (Figure S4) indicate a substantial preferred orientation that can be attributed to the diffraction from the comparably large single crystals that form on cooling from the melt (Figure S5). Therefore, the annealing temperature of 850 K was chosen, based on the LiMnBi thermal stability as determined from in situ HT-PXRD and considering the peritectic decomposition of the binary compound MnBi at 720 K.[39] Specifically, the chosen annealing temperature of 850 K is above the peritectic formation of MnBi (720 K) but below the decomposition of LiMnB (908 K).

The unit cell parameters obtained from Rietveld refinement of HT-PXRD data linearly increase upon heating (Figure 1). The coefficients of thermal expansion (CTE) obtained from linear fits of the data in the 300−700 K range resulted in the following values: CTE LiMnBi $(a) = \frac{da}{dT} \times \frac{1}{a} = 3.60(3) \times 10^{-5}$ K^{-1}, CTE LiMnBi $(c) = \frac{dc}{dT} \times \frac{1}{c} = 3.35(1) \times 10^{-5}$ K^{-1}, and CTE LiMnBi $(V) = \frac{dV}{dT} \times \frac{1}{V} = 1.09(1) \times 10^{-4}$ K^{-1}. The CTEs suggest isotropic structure expansion upon heating, as it was previously observed for the isostructural NaZbSb compound.[40]

Various loading molar ratios of Li:Mn:Bi were attempted to improve the yield of the LiMnBi phase (see the Experimental Section). The nearly single-phase sample with only ∼2 wt % Bi impurity as determined via Rietveld refinement and a trace amount of MnBi was obtained using the Li:Mn:Bi = 1.1:1.04:1 molar ratio and two-step annealing (Figure S3). These optimized synthesis conditions were used to prepare samples to measure magnetic properties and for controlled decomposition studies. We hypothesize that an excess of Li is needed to compensate for losses during partial evaporation at high temperatures while an excess of Mn could be due to the possible side reaction with crucible materials (Ta).

Structure and Magnetic Properties of LiMnBi. Alkali metal manganese pnictides *A*Mn*Pn* (*A* = Li−Cs; *Pn* = P−Bi) have a layered-like structure built from the alternating layers of the alkali metal *A* and [Mn*Pn*] layers composed of edge-sharing tetrahedra $MnPn_4$. LiMn(P, As, Sb) were reported to crystallize in the LaOF structure type, while the rest of *A*Mn*Pn*, including newly discovered LiMnBi, crystallize in the PbClF structure type (Figure 2). The distinct difference in the two

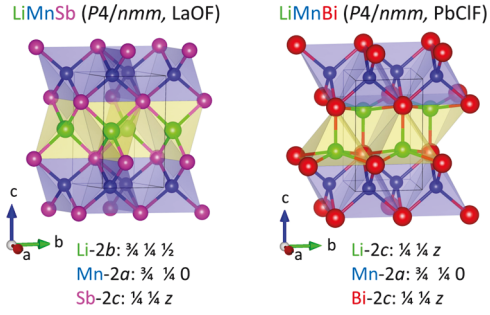

Figure 2. Crystal structures of compounds LiMnSb (*P*4/*nmm*, LaOF structure type) and LiMnBi (*P*4/*nmm*, PbClF structure type). $MnSb_4$ and $MnBi_4$ edge-shared distorted tetrahedra alternate with alkali metal atoms, which are inside the tetrahedra (LaOF type, yellow) or square pyramids (PbClF type, yellow) formed by *Pn* atoms. Li-green, Mn-blue, Sb-pink, and Bi-red. The standard setting for the *P*4/*nmm* space group is used with the cell origin at 2/*m*.

structure types is in the atomic coordinates of the alkali metal *A* causing a variation in the coordination environment of the alkali metal *A*: tetrahedral APn_4 in the LaOF structure type and square-pyramidal APn_5 in the case of the PbClF structure type (Figure 2, Table 1).

Magnetic structures were determined for most *A*Mn*Pn* compounds using neutron diffraction, with the exception of LiMnSb[2−4,41] and reported here LiMnBi. Two types of antiferromagnetic ordering of magnetic spins on Mn atoms were reported. The first type implies a magnetic unit cell coincident with the original tetragonal cell (Figure 3a) with the antiparallel alignment of Mn magnetic spins within the layer and parallel alignment of Mn spins between the adjacent [Mn*Pn*] layers. Such magnetic structure corresponds to nearest-neighbor antiferromagnetic (AFM) coupling of Mn spins in the *ab*-plane and ferromagnetic (FM) coupling between the layers, i.e., the C-type order. The second type

https://doi.org/10.1021/acs.chemmater.3c00140
Chem. Mater. 2023, 35, 3236−3248

Table 1. Structure Types among Alkali Metal Manganese Pnictides *AMnPn*[a]

AMnPn	P	As	Sb	Bi
Li	LaOF [1,3] *[C]	LaOF [1,2] *[G]	LaOF [1]	PbClF,[C] this work (calculations)
Na	PbClF [2]*[C]	PbClF [2]*[C]	PbClF [2]*[C]	PbClF [1,2]*[C]
K	PbClF [4]*[G]	PbClF [2]*[G]	PbClF [4]*[C]	PbClF [4]*[C]
Rb	PbClF [3,4]*[G]	PbClF [3,4]*[G]	PbClF [3]*[G]	PbClF [3,4]*[G]
Cs	PbClF [3,4]*[G]	PbClF [3]*[G]	PbClF [3]*[G]	PbClF [3,4]*[G]

[a]The asterisks indicate the type of magnetic structure experimentally determined from neutron diffraction studies, except for LiMnSb;[2−4] superscript C indicates that the magnetic unit cell is coincident with the nuclear tetragonal unit cell, i.e., C-type magnetic structure; and superscript G indicates that the magnetic unit cell is doubled in the *c*-direction compared to the nuclear tetragonal cell, i.e., G-type magnetic structure. The crystal structure type for LiMnSb was assigned based on PXRD data and no information about its magnetic structure is available.[1−4,22]

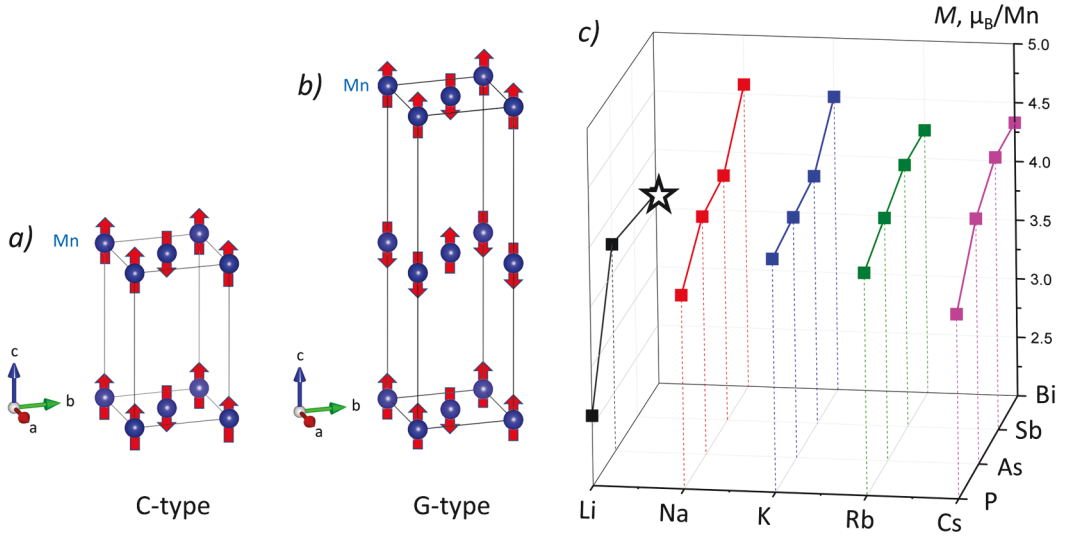

Figure 3. Two types of magnetic unit cells as determined from neutron diffraction studies[2−5] for the *AMnPn* family (A = Li−Cs; *Pn* = P−Bi). The antiferromagnetic ordering of Mn spins within the layer and ferromagnetic ordering of Mn spins between the layers result in the magnetic cell being identical to the nuclear tetragonal cell in (a), C-type magnetic structure; in (b) magnetic unit cell along the *c*-direction is doubled compared to the nuclear cell in the case of antiferromagnetic ordering of Mn spins within and between the layers, G-type magnetic structure; and (c) variation in the ordered magnetic moment, *M* (in μ_B per Mn atom) within the *AMnPn* family from neutron scattering experiments below 13 K.[2−4] No information about the magnetic structure of LiMnSb is available. For LiMnBi reported here, the magnetic moment from DFT calculations is added for comparison (star, this work). To be consistent with the literature,[2−4] the nonstandard settings for the *P*4/*nmm* space group were used with the cell origin placed at $\bar{4}m2$ and Mn atoms in the 2*a* site (0 0 0).

of ordering leads to the doubling of *c*-unit cell parameter in the magnetic unit cell compared to the nuclear unit cell due to the antiparallel alignment of Mn spins within and between layers (Figure 3b). Such magnetic structure is known as G-type and implies nearest-neighbor AFM coupling in the *ab*-plane and between the layers stacked along the *c*-axis. As can be seen from Table 1, there is a diagonal trend between these two types of magnetic structures within the *AMnPn* family. Interestingly, the magnitude of magnetic moment determined from neutron diffraction studies[2−4,41] increases within the LiMn*Pn*, NaMn*Pn*, KMn*Pn*, RbMn*Pn*, and CsMn*Pn* rows with increasing size of the pnictogen atom (Figure 3c). As the radius of *Pn* increases in the row P → As → Sb → Bi, the structure expands predominantly in the $a \times b$ plane at a greater rate compared to an expansion along the *c*-direction. Thus, the elongation of Mn−Mn distances within [Mn*Pn*] layers leads to the increase in the magnetic moment. An increase in the size of alkali ions in the row Li → Na → K → Rb → Cs leads to the expansion of the structure mainly along the *c*-direction. Therefore, the Mn−Mn distance between the [Mn*Pn*] layers increases, while Mn−Mn distances within the $a \times b$ plane increase only slightly.[4] The established dependence between Mn−Mn distances and the magnitude of the magnetic moment determined by neutron diffraction was first reported for NaMn*Pn*[2] and can be extended to the whole family,[2−4] including the new compound LiMnBi (Figure 3c).

Our theoretical calculations of the total and formation energies of the LiMnBi compound with two types of magnetic ordering are compiled in Table 2. Two models of the crystal structure are considered: LaOF type ($LiBi_4$ tetrahedral environment) and experimentally determined from SC-XRD data PbClF-type ($LiBi_5$ square-pyramidal environment) (Tables S1 and S2). Additionally, the possibility of FM or AFM ordering of spins on Mn atoms was considered. As can

Table 2. Calculated Total and Formation Energies of the LiMnBi Compound with LaOF or PbClF Type of Structure[a]

structure type	*E*, eV/atom		$E_{formation}$, eV/atom		*M*, μ_B per Mn atom	
	FM	AFM	FM	AFM	FM	AFM
LaOF	−4.848	−4.955	0.077	−0.030	4.055	3.944
PbClF	−4.969	−5.055	−0.046	−0.130	3.543	3.628

[a]Calculations were done considering FM or AFM ordering with the same magnetic cell as the nuclear cell (C-type shown in Figure 3a).

https://doi.org/10.1021/acs.chemmater.3c00140
Chem. Mater. 2023, 35, 3236−3248

be seen from Table 2, the PbClF type of structure with AFM ordering has the lowest energy. The total energy of the AFM structure (E = −5.055 eV/atom) with the same magnetic cell as the nuclear tetragonal unit cell (C-type magnetic structure shown in Figure 3a) is slightly lower than the total energy (E = −5.052 eV/atom) of the AFM structure with the doubled c (G-type magnetic structure shown in Figure 3b). The DFT calculated magnetic moment per Mn atom in LiMnBi with a C-type magnetic structure amounts to 3.628 μ_B, which is consistent with the general trend of increasing magnetic moment with the size of the *Pn* atom established for the *A*Mn*Pn* family from neutron diffraction (Figure 3c).

Magnetic properties of two LiMnBi polycrystalline samples (sample 1 and sample 2) were measured (Figures 4, S6 and S7). Both samples contained LiMnBi as a major phase, 2 wt % of Bi, and a trace amount of MnBi (Figure S3). Samples were stored and handled in a glovebox prior to data collection, yet, as we will show below, LiMnBi is extremely air-sensitive and decomposes to yield MnBi even in the presence of a trace amount of oxygen gas. Sample 1 was used for initial, below 300 K, magnetization measurements as well as for solid-state ^{7}Li NMR data collection (vide infra), while sample 2 was used to measure magnetic properties over a wider temperature range, i.e., above room temperature. As can be seen from the field- and temperature-dependent magnetization data for samples 1 and 2 (Figure 4) that both LiMnBi samples show similar behavior, with no superconductivity detected down to 5 K. The field dependence of magnetization at the magnetic field above 1 T is linear with no tendency for saturation. The clear deviation from linearity of the field dependence of magnetization at a low magnetic field (0−10,000 Oe) is attributed to a ferromagnetic impurity, assumed to be MnBi (saturation magnetization of 81.3 emu/g, $T_c \approx 630$ K[42]). From the intercept of the linear fit above 1 T of $M(H)$ at 300 K and using the literature data for saturation magnetization,[42] the content of ferromagnetic MnBi impurity was estimated to be 0.03 wt % in both samples. The ferromagnetic impurity is also manifested in the field dependence of M/H vs T plots for sample 1 (Figure S6a). Using the Honda−Owen method,[43,44] we estimated the amount of MnBi to be 0.1 wt % based on its literature $M(H)$ data[42,45] (Figure S6a). Since both samples have pronounced contributions from the MnBi impurity phase, any attempt at a Curie−Weiss analysis M/H vs T data in the 150−245 K range (even using Honda−Owen analysis) gives nonphysically small values for Mn moments (see Figures S6 and S7 and the Supporting Information for further discussion). The below-room-temperature data strongly suggested that there might be an AFM order of the Mn sublattice taking place above room temperature. Indeed, when ^{7}Li solid-state NMR (see below) and magnetization data were collected for temperatures above 340 K (Figures 4b and S6a), a clear signature of antiferromagnetic ordering emerged. This AFM ordering above room temperature resembles that in $AlMn_2B_2$, where solid-state NMR was used to unambiguously detect the transition above room temperature.[46]

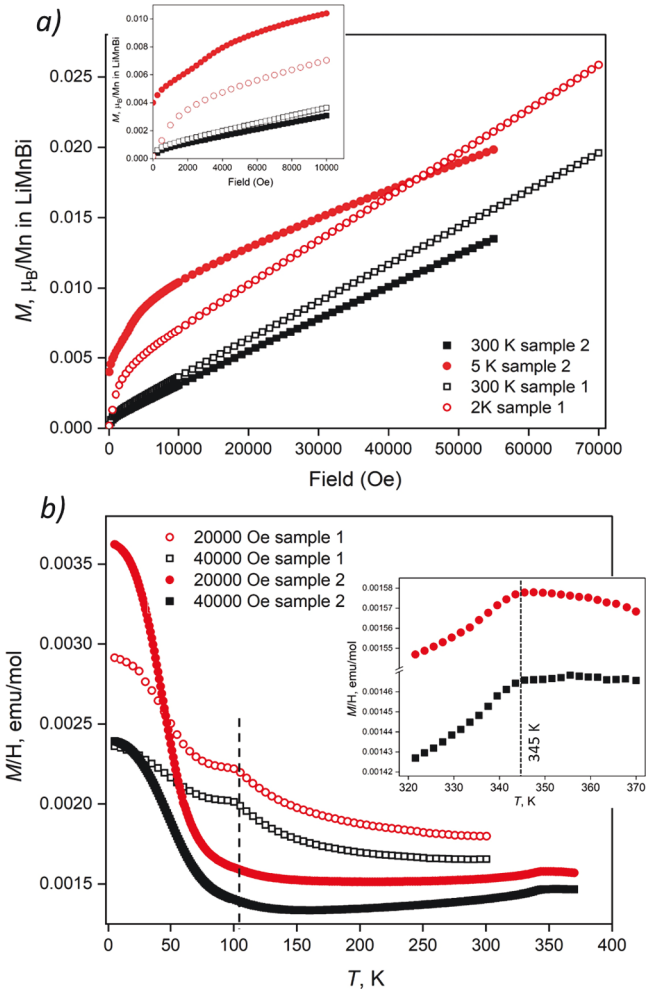

Figure 4. Magnetic properties of LiMnBi samples. (a) Field dependence of magnetization, M, in μ_B per Mn atom at 2 K (sample 1), 5 K (sample 2), and 300 K (samples 1 and 2). (b) Temperature dependence of M/H between 2 and 370 K with the inset showing a transition at 345 K.

Solid-State ^{7}Li NMR. To further probe magnetic ordering in LiMnBi, we collected solid-state ^{7}Li NMR data for the same sample as was used for magnetic measurements (sample 1 from above). Temperature dependence of the representative ^{7}Li-NMR spectra in the temperature range 8−469 K is shown in Figure 5a. The spectra above 345 K are observed around zero NMR shift shown by the dashed line and are very sharp with a full width at half maximum (FWHM) of ∼25 kHz (∼15 Oe). For the I = 3/2 nuclei, one may expect three spectral lines in the presence of quadrupole effects: one central (I_z = 1/2 ↔ 1/2) and two satellite transitions (I_z = 3/2 ↔ 1/2 and − 3/2 ↔ −1/2). The observed single-line shape indicates the small quadrupole interaction whose upper limit is estimated to be 100 kHz from the observed spectra at high temperatures. Upon cooling just below 342 K, a drastic broadening of the NMR spectra is observed, indicating a magnetic phase transition. Since no obvious change in the peak position below 342 K is observed, the magnetic state is considered to be AFM. Similar broad NMR spectra in the AFM state have been observed in $AlMn_2B_2$.[46] The inset shows the temperature dependence of the FWHM where the clear increase of FWHM on cooling is evident around the magnetic phase transition temperature T_N ∼ 342 K. It is noted that no clear change in FWHM can be detected around either 100 or 50 K. These results suggest that the features detected in the temperature-dependent magnetization near ∼100 K and again at ∼50 K (Figures S6 and S7) are either completely suppressed by the application of an external magnetic field (H ∼ 7.4 T) or the anomalies associated with impurity phases contain no Li. Taken together

https://doi.org/10.1021/acs.chemmater.3c00140
Chem. Mater. 2023, 35, 3236−3248

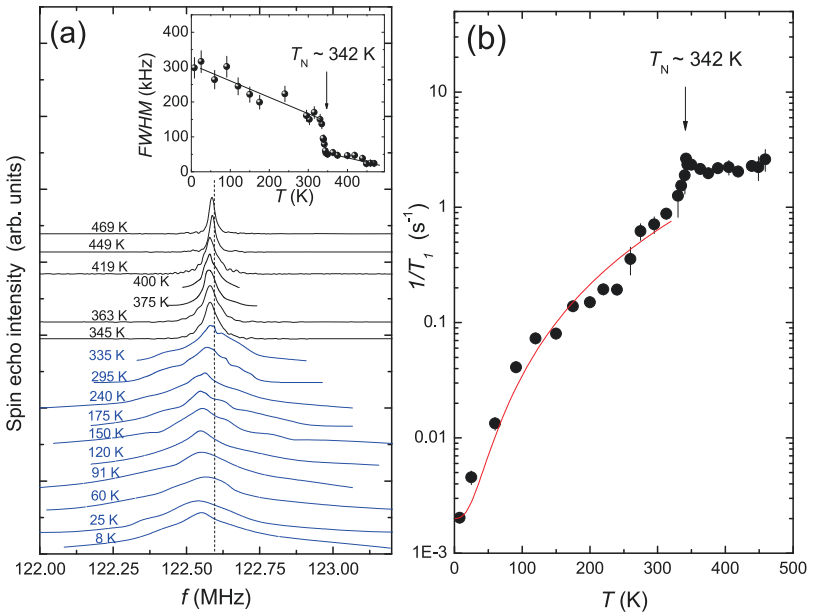

Figure 5. (a) Temperature dependence of ^{7}Li-NMR spectra. Spectra in the paramagnetic state are shown in black whereas those in the magnetic state are shown in blue. The dashed line corresponds to the zero shift frequency for ^{7}Li at an applied field of 7.4089 T. Inset: the temperature dependence of FWHM. A drastic change in FWHM is observed around $T_N \sim 342$ K. The straight lines are guides for the eye. (b) Temperature dependence of the ^{7}Li spin−lattice relaxation rate ($1/T_1$). The red curve shows $1/T_1 = 1.3 \times 10^{-7}\ T^{2.7} + 0.002$ (1/s) where the first term originates from the two-magnon relaxation process in antiferromagnets and the second term is due to impurities.

with the magnetization data, a MnBi impurity ($M_{saturation}$ = 81.3 emu/g, $T_c \approx 630$ K[42]) is the most likely explanation.

To obtain further insights into the magnetic properties of LiMnBi, we have also measured $1/T_1$ for temperature dependence (Figure 5b). With decreasing temperature from 450 to 360 K, $1/T_1$ is nearly independent of temperature, which is attributed to the paramagnetic fluctuations of the Mn spin. With further lowering of the temperature below 360 K, $1/T_1$ starts to increase and exhibits a clear peak at $T_N \sim 342$ K. This is due to the critical slowing down of the Mn spin fluctuations, indicating that the AFM phase transition is a second-order phase transition. Below $T_N \sim 342$ K, $1/T_1$ shows a strong temperature dependence where $1/T_1$ roughly follows a $T^{2.7}$ power-law behavior. This power-law dependence of $1/T_1$ is close to T^3 expected for the two-magnon scattering process for antiferromagnets.[47] A deviation from the power-law behavior below 20 K was observed, which is likely due to relaxation associated with impurities giving a temperature-independent $1/T_1$. The red curve in Figure 5b is the calculated temperature dependence of $1/T_1$ with the two contributions to $1/T_1$ from the magnon scattering and impurity effect, which seems to reproduce the experimental data. Finally, it is noted that no clear anomaly in $1/T_1$ around either 100 K or 50 K is detected as in the case of NMR spectrum measurements, indicating again that the magnetic anomaly in the magnetization measurements is completely suppressed due to the external field or is due to impurities.

All in all, magnetic property measurements of two polycrystalline LiMnBi samples together with solid-state ^{7}Li NMR data suggest that the Mn sublattice in LiMnBi orders antiferromagnetically below $T_N \sim 340$ K, while the low-temperature features in magnetic data are attributed to the trace amount of secondary phases, including ferromagnetic MnBi. Interestingly, variable-temperature neutron diffraction data for selected representatives of the *A*Mn*Pn* family indicate an AFM ordering of Mn atoms above room temperature for isostructural NaMnBi and NaMnSb (293 K < T_N < 383 K), KMnAs (393 K < T_N < 423 K), NaMnAs (293 K < T_N < 633 K), and NaMnP (293 K < T_N < 593 K),[2] as well as structurally different LiMnAs (T_N = 374 K),[41] while the temperature-variable neutron diffraction data needed to unambiguously determine the transition temperature range for other *A*Mn*Pn* representatives are lacking.[2−4]

Controlled Decomposition of LiMnBi to MnBi Ferromagnet. We further studied the reactivity of LiMnBi in various chemical environments and found out that by controlling the rate of the LiMnBi decomposition, it is possible to stabilize the MnBi product with the hexagonal NiAs structure type ($P6_3/mmc$). MnBi is one of the strongest rare-earth-metal-free ferromagnets.[42,45,48−59] The chosen synthesis method tremendously impacts the magnetic properties of MnBi. The reported synthesis methods include continuous spinning arc melting, rapid solidification, reannealing, ball-milling, and high-temperature solution growth of single crystals.[42,49−59] The purity of the target stoichiometric MnBi varies from 50% to essentially 100% for single-crystal growth. Synthetic challenges are attributed to the complex peritectic Mn−Bi phase diagram[39] that implies crystallization of the *ht*-$Mn_{2.23}Bi_{1.88}$ compound (Mn:Bi ∼ 1.19:1) prior to the formation of MnBi. While stoichiometric MnBi is a strong ferromagnet, the compositionally similar *ht*-$Mn_{2.23}Bi_{1.88}$ is paramagnetic.[45,48,58,59]

We studied LiMnBi decomposition in air, in deionized water and ethanol, and in aprotic polar solvents, including acetonitrile, ethylenediamine, pyridine, DMF, and DMSO. As it will be shown below, the yield of MnBi strongly depends on the type of reagents and kinetics of the reaction: a slow rate and mild reaction media lead to a high fraction of the MnBi product (∼80 wt %). PXRD data (Figure 6) show that LiMnBi reacts with moisture and oxygen and decomposes to MnBi and, presumably, amorphous lithium hydroxide (not detected by laboratory PXRD). The basic pH (10−11) of the solution

https://doi.org/10.1021/acs.chemmater.3c00140
Chem. Mater. 2023, 35, 3236−3248

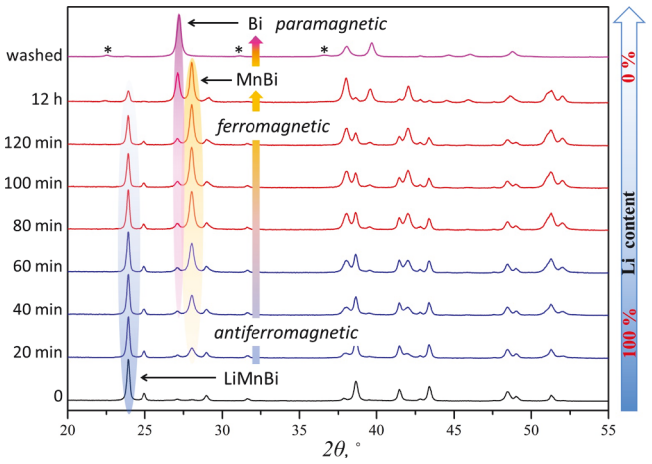

Figure 6. PXRD patterns show that upon exposure to air, LiMnBi (bottom, black; the representative diffraction peak is highlighted in blue) slowly decomposes into ferromagnetic MnBi (peak highlighted in yellow), which in turn, hydrolyzes, yielding Bi (diffraction peak highlighted in pink) and traces of $Mn(OH)_2$ (diffraction peaks marked with *).

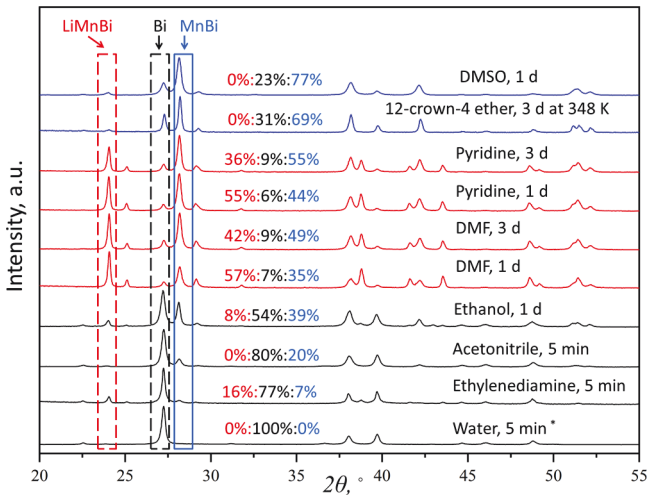

Figure 7. PXRD patterns show the outcome of delithiation of the LiMnBi phase in different solvents. The most intense diffraction peaks of LiMnBi, Bi, and MnBi phases and their relative weight fractions (wt %) from Rietveld refinement of PXRD data are shown in red, black, and blue, respectively.

obtained by rinsing LiMnBi powder with DI water is consistent with $LiOH/Li_2O$ formation. The delithiation of LiMnBi is relatively fast during the first hour (Figure 6, PXRD patterns in blue). The delithiation slows down afterward, and after 12 h of exposure to air, nearly all of LiMnBi is decomposed. Simultaneously, hydrolysis of binary MnBi occurs leading to an increase in the fraction of elemental Bi. The PXRD pattern of the sample after washing with water contains Bi as a major crystalline phase and possibly traces of $Mn(OH)_2$ (mostly amorphous and indetectable by PXRD). As a result, LiMnBi → MnBi → Bi chemical transformation under aerobic conditions is accompanied by the variation in room-temperature magnetism: antiferromagnet → ferromagnet → paramagnet. After 12 h of exposure to air, the weight fractions of the crystalline phases determined from Rietveld refinement of PXRD data are LiMnBi:MnBi:Bi = 11 wt %:55 wt %:34 wt %.

The rate of delithiation in LiMnBi and the subsequent hydrolysis of MnBi can be controlled by the chemical environment (Figure 7), for instance, by the type of organic solvent used under anaerobic conditions. The LiMnBi compound reacts vigorously and immediately with water, acetonitrile, and ethylenediamine yielding Bi as the main crystalline product (>75 wt %). The reactions with ethanol, DMF, DMSO, and pyridine are considerably slower and, therefore, were carried out for 1 day. As can be seen from Figure 7 the fraction of MnBi increases from 35 to 77 wt % in a row DMF → ethanol → pyridine → DMSO. Yet, the decomposition in ethanol and DMSO is faster, thus leading to a considerable fraction of Bi (54 and 23 wt %, respectively), whereas decomposition in DMF and pyridine is slower, resulting in a considerable amount of LiMnBi that remained after the 1 day exposure (57 and 55 wt %). Therefore, the exposure time in DMF and pyridine was extended to 3 days, which only slightly increased the MnBi fraction (from 35 to 49 wt % in DMF and from 44 to 55 wt % in pyridine); however, the Bi fraction increased as well (up to 9 wt %), and a significant amount of unreacted LiMnBi was still present. We then attempted a reaction between LiMnBi and 12-crown-4 ether (boiling point 343 K), which is a ligand known to selectively bind various cations, particularly Li^+. After 3 days at an elevated temperature of ∼348 K, the LiMnBi-to-MnBi transformation was complete, but a sample contained a considerable fraction of Bi impurity (31 wt %). To sum up, the speed of Li^+ leaving the LiMnBi structure defines the reaction outcome. If the Li "removal" is fast (as in water, ethanol, acetonitrile, and ethylenediamine), then the major crystalline phase is elemental Bi. For the slower rate of delithiation (DMF and pyridine), a significant fraction of LiMnBi leftover is still present even after 3 days. However, even if delithiation is slow enough to be accomplished within 1 day (DMSO and 12-crown-4 ether), the competing side reaction leads to 20−30 wt % of Bi impurity. Therefore, none of the attempted reactions resulted in a yield of the MnBi product exceeding 77 wt %.

To study the kinetics of LiMnBi-to-MnBi transformation, we then subjected LiMnBi to a trace amount of oxygen in a glovebox with $p(O_2)$ < 1 ppm and $p(H_2O)$ < 1 ppm (Figure 8). At room temperature, the reaction is extremely slow. Around 2 months is needed to achieve ∼87 wt % fraction of MnBi by controlled LiMnBi decomposition (Figure 8a). The precursor LiMnBi contained ∼3 wt % of Bi impurity initially, and its amount only slightly increased to ∼4 wt % after 2 months. Exposure of a sample in a glovebox for longer than 50 days did not result in complete decomposition, since ∼10 wt % of LiMnBi was still present. In turn, the MnBi fraction started to slowly decrease leading to the increase in the Bi content, indicating MnBi decomposition.

To achieve a complete LiMnBi-to-MnBi transformation, an experiment was carried out in a glovebox at elevated temperatures (Figure 8b). The sample of LiMnBi was kept on a hot plate at room temperature for the first 4 days for reference (Figure 8b, region I highlighted in pink). Afterward, the temperature was raised to 398 K, which resulted in an increase in the reaction rate (Figure 8b, region II in green). Even though 78 wt % fraction of MnBi was achieved within 17 days, an increase in the decomposition rate causes an increase in the amount of the Bi side product (from 3 to 7 wt %). Neither further exposure (Figure 8b, region III in blue) at the same temperature nor regrinding of the sample in a mortar and pestle (Figure 8b, region IV in pale yellow) promoted

https://doi.org/10.1021/acs.chemmater.3c00140
Chem. Mater. 2023, 35, 3236−3248

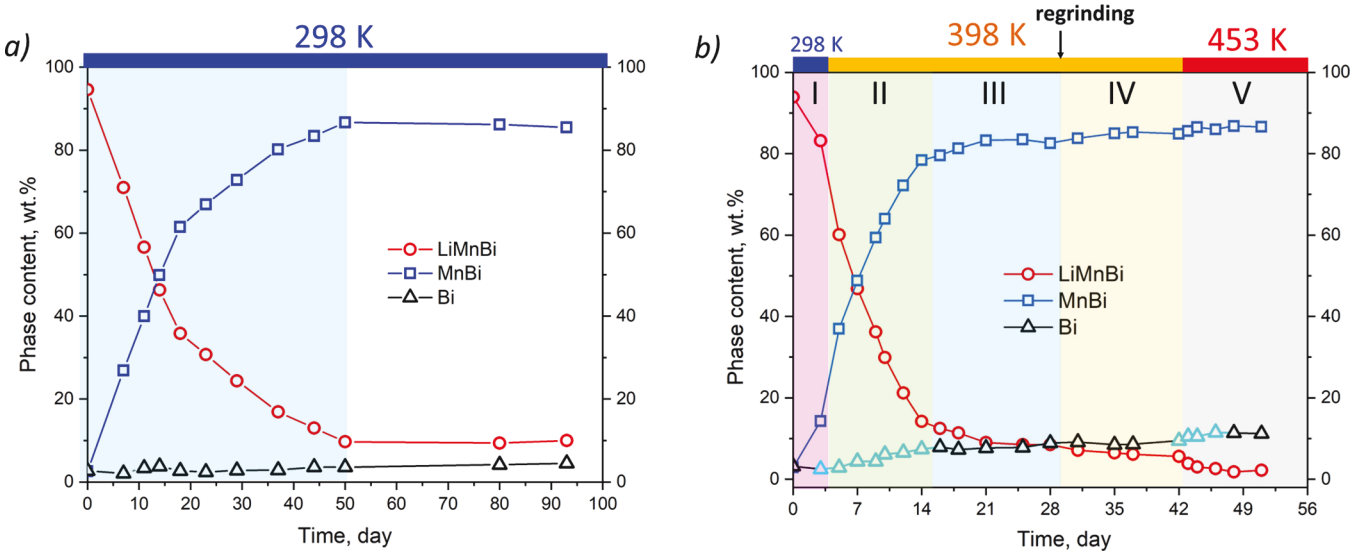

Figure 8. Variation of phase fractions (wt %) of LiMnBi (red circles), MnBi (blue squares), and Bi (black triangles) in the sample exposed to trace amounts of O_2/H_2O in a glovebox at room temperature (298 K) (a) and at elevated temperatures (398 K/453 K). Regions of various rates of the decomposition process are highlighted in light blue in (a) and I-pink, II-green, III-light blue, IV-pale yellow, and V-gray in (b). Cyan triangles are used to highlight regions where Bi wt % rapidly increases.

subsequent LiMnBi decomposition or formation of additional Bi. We presume that the remaining particles of LiMnBi are heavily coated with Li_2O inhibiting O_2 diffusion, thus Li extraction. A further increase in temperature to 453 K (Figure 8b, region V in gray) leads to a slight increase in the reaction rate with the subsequent increase in the Bi fraction. Overall, LiMnBi decomposition in a glovebox at room temperature (Figure 8a, MnBi: 86.7 wt %; Bi: 3.6 wt %; LiMnBi: 9.7 wt %) and at elevated temperatures (Figure 8b, MnBi: 86.6 wt %; Bi: 11.2 wt %; LiMnBi: 2.2 wt %) resulted in a weight fraction of MnBi as high as 87 wt %. However, it should be mentioned that Rietveld refinement of PXRD provides the relative wt % of the crystalline phases only. If the expected stoichiometric amounts of amorphous phases Li_2O and MnO_2 are considered, the fraction of MnBi is reduced to 82.4 wt % for the decomposition carried out at room temperature (MnBi: 82.4 wt %; Bi:3.4 wt %; LiMnBi: 9.2 wt %; Li_2O: 4.6 wt %; MnO_2: 0.3 wt %) and to 79.8 wt % for the decomposition at elevated temperatures (MnBi: 79.8 wt %; Bi: 10.3 wt %; LiMnBi: 2.0 wt %; Li_2O: 4.9 wt %; MnO_2: 3.0 wt %).

To test whether the delithiation of LiMnBi yielding ferromagnetic MnBi is exclusive to the LiMnBi compound, we studied a decomposition of the isostructural NaMnBi and KMnBi compounds as well as the structurally related $CaMn_2Bi_2$. Neither of them yielded MnBi. More reactive isostructural NaMnBi and KMnBi compounds showed a rapid decomposition in air, yielding only elemental Bi as a crystalline product, while $CaMn_2Bi_2$ is quite stable in air. The formation of MnBi ferromagnets from antiferromagnetic LiMnBi can be understood considering their crystal structures, as proposed by the following simplistic mechanism (Figure 9). After a complete Li deintercalation from LiMnBi, the resulting [MnBi] layers condense and subsequently distort to yield 3D hexagonal structures of MnBi (Figure 9). Notably, a Mn−Mn distance of 3.1 Å within the square nets in the LiMnBi structure is identical to the shortest Mn−Mn distance in the hexagonal MnBi structure. As it was shown above (Figures 6, 7, and 8), Bi is a side product of LiMnBi decomposition (in addition to presumably amorphous manganese and lithium

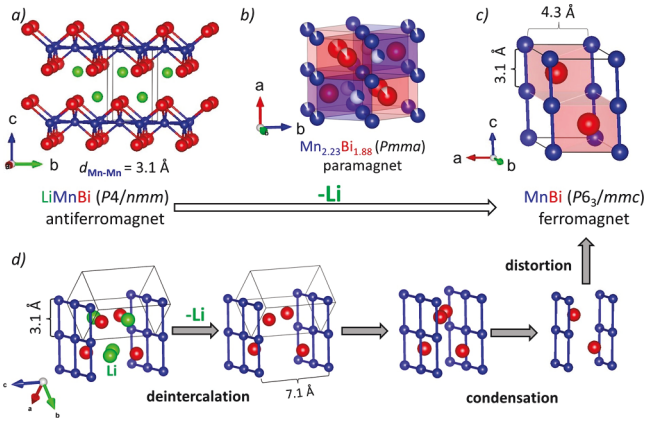

Figure 9. (a) Crystal structure of LiMnBi highlighting square nets of Mn atoms capped by Bi atoms; Li − green, Mn − blue, and Bi − red spheres and (b) crystal structure of $Mn_{2.33}Bi_{1.88}$. Atoms partially occupying sites are shown as partially filled spheres. (c) Crystal structure of MnBi and (d) proposed mechanism of LiMnBi decomposition yielding MnBi. The schematic includes Li-layer "removal" (deintercalation), condensation of the Mn square nets with d_{Mn-Mn} = 3.1 Å, and subsequent formation of the hexagonal MnBi structure; Mn−Bi bonds are omitted for clarity.

oxides/hydroxides that are not detectable from PXRD); thus, the Bi formation rate is proportional to the speed of the reaction. If the speed of Li deintercalation from the LiMnBi structure (the first step in the proposed mechanism, Figure 9a) is slow (as at room temperature), the condensation of the [MnBi] layers leads to the MnBi structure. However, if the reaction speed is too rapid, a lot of "faults" during the [MnBi] condensation occur, and a fraction of [MnBi] layers can be oxidized prior to the condensation, yielding elemental Bi and manganese oxide. Considering this, lower reactivity due to a shorter interlayer [MnBi] distance of 7.1 Å (Figure 9) in LiMnBi compared to isostructural NaMnBi (7.7 Å) and KMnBi (8.3 Å) can explain the formation of MnBi only in the case of LiMnBi, but not for the Na- and K-analogues.

https://doi.org/10.1021/acs.chemmater.3c00140
Chem. Mater. 2023, 35, 3236−3248

Scanning electron microscopy (SEM) images using BSE and SE modes were collected for the powdered sample that contains up to 82 wt % MnBi and was prepared by controlled decomposition of LiMnBi in a glovebox for an extended period of time at room temperature. As can be seen from Figure 10a,

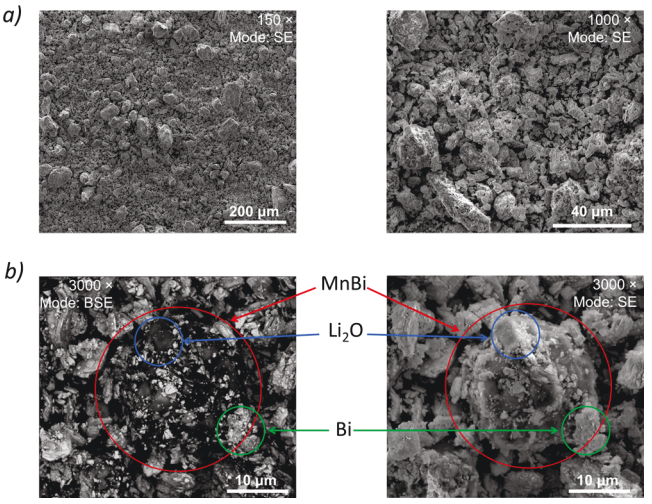

Figure 10. SEM images obtained in BSE and SE modes for a sample of LiMnBi kept in a glovebox for an extended period of time (the sample contains up to 82 wt % MnBi). (a) Images show the variation in the particle size and (b) MnBi particle coated with lithium oxide (white in the SE image and dark in the BSE image) and elemental Bi (gray in the SE image and white in the BSE image).

the samples show the variation in the particle size between 5 and 50 μm. MnBi particles are heavily coated with (presumably) lithium oxide and elemental Bi (Figure 10b). EDXS analysis confirmed the expected Mn:Bi = 1:1 molar ratio. The saturation magnetization (Figure 11a) of the LiMnBi sample oxidized in a glovebox (containing up to 82 wt % MnBi) is in the 35−40 emu/g (1.6−1.9 μ_B/Mn) range at 300 and 2 K, which is about 50% of the expected value of 81.3 emu/g (~3.8 μ_B/Mn) for pure and fully dense MnBi samples at 300 K[42] or high-quality single crystals (3.6−4.1 μ_B/Mn).[45] The saturation magnetization is slightly higher for the sample oxidized on a hot plate at 453 K as compared to the sample kept at room temperature (Figures 8a,b and 11a). A comparably low value of saturation magnetization is not unexpected for the "as-prepared" MnBi, since postprocessing (e.g., ball-milling and particle size optimization combined with heat treatment[42,58]) is required to obtain a high-performance permanent magnet. The temperature dependence of M/H between 5 and 300 K of the MnBi sample prepared by decomposition of LiMnBi in a glovebox is shown in Figure 11b. These data are in good agreement with the literature,[42,45,49,50] suggesting that MnBi obtained via LiMnBi decomposition has the same spin reorientation transition at 90−100 K as MnBi prepared by other routes.

CONCLUSIONS

The intermetallic compound LiMnBi is a newly discovered member of the *A*Mn*Pn* family (*A* = alkali metal; *Pn* = pnictogen). LiMnBi has a layered PbClF type of crystal structure that is common for *A*Mn*Pn* compounds. The structure is built of alternating Li and [MnBi] layers with Mn tetrahedrally coordinated to four Bi atoms within the layer. LiMnBi was synthesized by two-step annealing of elements with the annealing temperature chosen based on in situ PXRD data. DFT calculations predict that the PbClF type of structure with AFM ordering of Mn spins and the magnetic unit cell that is coincident with the nuclear cell has the lowest energy. DFT calculated magnetic moment on Mn atoms in the AFM structure of LiMnBi at 0 K is in agreement with the previously established trend for the *A*Mn*Pn* family between magnetic moment and Mn−Mn interatomic distances. Magnetic property measurements and solid-state ^{7}Li NMR data collected for polycrystalline LiMnBi samples indicate the long-range antiferromagnetic ordering of the Mn sublattice at ~340 K, with no superconductivity detected down to 5 K.

LiMnBi is air- and water-sensitive. The study of the controlled LiMnBi decomposition in air indicates LiMnBi → MnBi → Bi transformation with a concurrent change in magnetic properties as antiferromagnet → ferromagnet → paramagnet. Such decomposition is exclusive for LiMnBi, since neither isostructural NaMnBi and KMnBi compounds nor structurally related $CaMn_2Bi_2$ yield MnBi upon decomposition.

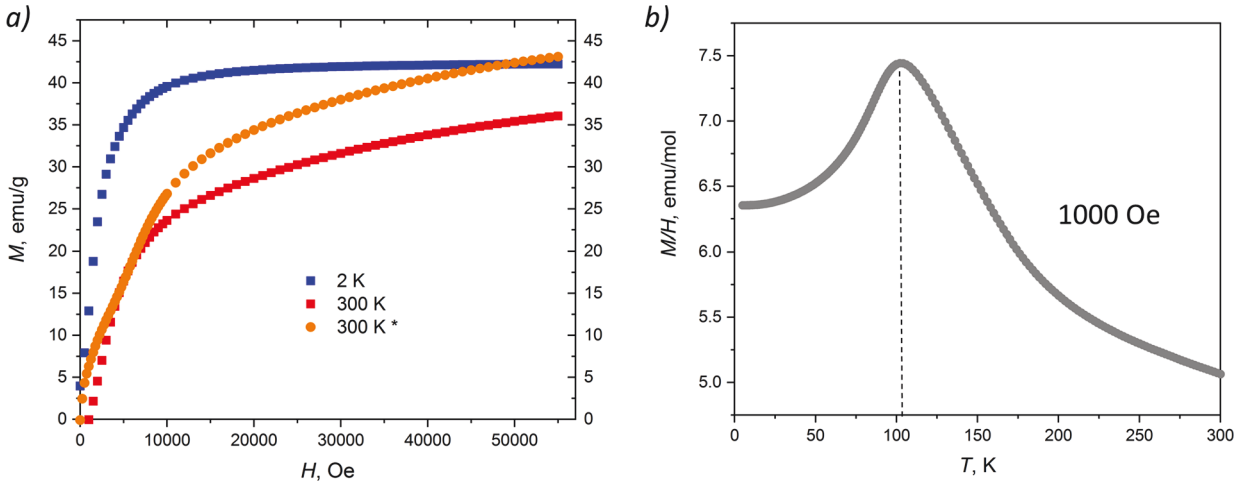

Figure 11. (a) Magnetization M vs magnetic field and (b) temperature dependence of M/H vs T (right) of the "as-prepared" MnBi polycrystalline sample obtained by controlled decomposition of LiMnBi in a glovebox. Additionally, M vs magnetic field (orange curve*) for the sample heated to 453 K in a glovebox is shown in (a).

https://doi.org/10.1021/acs.chemmater.3c00140
Chem. Mater. 2023, 35, 3236−3248

Delithiation in LiMnBi proceeds in various organic solvents and under anaerobic conditions, while the MnBi yield depends on the type of solvent used and kinetics of the reaction. A slow decomposition in the mild reaction media leads to a high fraction of the product (up to 82 wt %). The saturation magnetization of the "as-prepared" MnBi is ∼50% of the expected value of 81.3 emu/g, yet it is known that postprocessing is required to obtain MnBi-based permanent magnets with high performance. Overall, this study enriches the chemistry of ternary pnictides and showcases an example of using soft-chemistry methods to obtain difficult-to-synthesize compounds.

■ ASSOCIATED CONTENT

Supporting Information

The Supporting Information is available free of charge at https://pubs.acs.org/doi/10.1021/acs.chemmater.3c00140.

Crystallographic data of LiMnBi (CIF)

Additional tables, Rietveld refinement plots, PXRD patterns, magnetic data, and tables with parameters of XRD data collection and refinement (PDF)

■ AUTHOR INFORMATION

Corresponding Author

Julia V. Zaikina − *Department of Chemistry, Iowa State University, Ames, Iowa 50011, United States;* orcid.org/0000-0002-8755-1926; Email: yzaikina@iastate.edu

Authors

Volodymyr Gvozdetskyi − *Department of Chemistry, Iowa State University, Ames, Iowa 50011, United States;* Present Address: Department of Chemistry, University of Alberta, Edmonton, Alberta T6G 2G2, Canada (V.G.)

Khusboo Rana − *Department of Physics and Astronomy and Ames National Laboratory, US DOE, Iowa State University, Ames, Iowa 50011, United States*

Raquel A. Ribeiro − *Department of Physics and Astronomy, Iowa State University, Ames, Iowa 50011, United States*

Aishwarya Mantravadi − *Department of Chemistry, Iowa State University, Ames, Iowa 50011, United States*

Adedoyin N. Adeyemi − *Department of Chemistry, Iowa State University, Ames, Iowa 50011, United States*

Renhai Wang − *School of Physics and Optoelectronic Engineering, Guangdong University of Technology, Guangzhou 510006, China*

Huafeng Dong − *School of Physics and Optoelectronic Engineering, Guangdong University of Technology, Guangzhou 510006, China*

Kai-Ming Ho − *Department of Physics and Astronomy, Iowa State University, Ames, Iowa 50011, United States*

Yuji Furukawa − *Department of Physics and Astronomy and Ames National Laboratory, US DOE, Iowa State University, Ames, Iowa 50011, United States*

Paul C. Canfield − *Department of Physics and Astronomy and Ames National Laboratory, US DOE, Iowa State University, Ames, Iowa 50011, United States*

Complete contact information is available at: https://pubs.acs.org/10.1021/acs.chemmater.3c00140

Funding

Financial support from the National Science Foundation (DMR-1944551) CAREER award is gratefully acknowledged. The work at Ames Laboratory was supported by the U.S. Department of Energy (DOE), Office of Science, Basic Energy Sciences, Materials Science and Engineering Division, under Contract No. DE-AC02-07CH11358, including a grant of computer time at the National Energy Research Scientific Computing Center (NERSC) in Berkeley, CA. Use of the Advanced Photon Source at Argonne National Laboratory was supported by the U.S. Department of Energy, Office of Science, Office of Basic Energy Sciences, under Contract No. DE-AC02-06CH11357. RAR is supported by the Gordon and Betty Moore Foundation's EPiQS Initiative through Grant No. GBMF4411. Work at Guangdong University of Technology was supported by the Guangdong Basic and Applied Basic Research Foundation (Grant Nos. 2021A1515110328 and 2022A1515012174).

Notes

The authors declare no competing financial interest.

■ ACKNOWLEDGMENTS

We thank Dr. Wenqian Xu and Dr. Andrey Yakovenko at 17-BM beamline, APS ANL, for help with high-temperature synchrotron powder XRD data collection.

■ REFERENCES

(1) Achenbach, G. D.; Schuster, H. U. Ternäre Verbindungen des Lithiums und Natriums mit Mangan und Elementen der 5. Hauptgruppe. *Z. Anorg. Allg. Chem.* **1981**, *475*, 9−17.

(2) Bonger, W.; Müller, P.; Höppner, R.; Schuster, H. U. Zur Charakterisierung der magnetischen Eigenschaften von NaMnP, NaMnAs, NaMnSb, NaMnBi, LiMnAs und KMnAs über Neutronenbeugungsexperimente. *Z. Anorg. Allg. Chem.* **1986**, *539*, 175−182.

(3) Müller, R.; Kuckel, M.; Schuster, H.; Müller, P.; Bronger, W. Neue AMnX-Verbindungen mit A= Rb, Cs und X = P, As, Sb, Bi: Struktur und Magnetismus. *J. Alloys Compd.* **1991**, *176*, 167−172.

(4) Schucht, F.; Dascoulidou, A.; Mueller, R.; Jung, W.; Schuster, H. U.; Bronger, W.; Mueller, P. Die magnetischen Eigenschaften der Alkalimetall-Manganpnictide KMnP, RbMnP, CsMnP, RbMnAs, KMnSb, KMnBi, RbMnBi und CsMnBi Neutronenbeugungsuntersuchungen und SuszeptibilitaÈtsmessungen. *Z. Anorg. Allg. Chem.* **1999**, *625*, 31−36.

(5) Kamihara, Y.; Hiramatsu, H.; Hirano, M.; Kawamura, R.; Yanagi, H.; Kamiya, T.; Hosono, H. Iron-based layered superconductor: LaOFeP. *J. Am. Chem. Soc.* **2006**, *128*, 10012−10013.

(6) Ishida, K.; Nakai, Y.; Hosono, H. To what extent iron-pnictide new superconductors have been clarified: a progress report. *J. Phys. Soc. Jpn.* **2009**, *78*, No. 062001.

(7) Canfield, P. C.; Bud'ko, S. L. FeAs-Based Superconductivity: A Case Study of the Effects of Transition Metal Doping on $BaFe_2As_2$. *Annu. Rev. Condens. Matter Phys.* **2010**, *1*, 27−50.

(8) Tanabe, K.; Hosono, H. Frontiers of research on iron-based superconductors toward their application. *Jpn. J. Appl. Phys.* **2012**, *51*, No. 010005.

(9) Hosono, H.; Kuroki, K. Iron-based superconductors: current status of materials and pairing mechanism. *Phys. C* **2015**, *514*, 399−422.

(10) Si, Q.; Yu, R.; Abrahams, E. High-temperature superconductivity in iron pnictides and chalcogenides. *Nat. Rev. Mater.* **2016**, *1*, 16017.

(11) Johnston, D. C. The puzzle of high temperature superconductivity in layered iron pnictides and chalcogenides. *Adv. Phys.* **2010**, *59*, 803−1061.

(12) Park, T.; Park, E.; Lee, H.; Klimczuk, T.; Bauer, E. D.; Ronning, F.; Thompson, J. D. Pressure-induced superconductivity in $CaFe_2As_2$. *J. Phys.: Condens. Matter* **2008**, *20*, No. 322204.

(13) Torikachvili, M. S.; Bud'ko, S. L.; Ni, N.; Canfield, P. C. Pressure induced superconductivity in $CaFe_2As_2$. *Phys. Rev. Lett.* **2008**, *101*, No. 057006.
(14) Canfield, P. C.; Bud'ko, S. L.; Ni, N.; Kreyssig, A.; Goldman, A. I.; McQueeney, R. J.; Torikachvili, M. S.; Argyriou, D. N.; Luke, G.; Yu, W. Structural, magnetic and superconducting phase transitions in $CaFe_2As_2$ under ambient and applied pressure. *Phys. C* **2009**, *469*, 404−412.
(15) Iyo, A.; Kawashima, K.; Kinjo, T.; Nishio, T.; Ishida, S.; Fujihisa, H.; Gotoh, Y.; Kihou, K.; Eisaki, H.; Yoshida, Y. New-Structure-Type Fe-Based Superconductors: $CaAFe_4As_4$ (A = K, Rb, Cs) and $SrAFe_4As_4$ (A = Rb, Cs). *J. Am. Chem. Soc.* **2016**, *138*, 3410−3415.
(16) Singh, S. J.; Bristow, M.; Meier, W. R.; Taylor, P.; Blundell, S. J.; Canfield, P. C.; Coldea, A. I. Ultrahigh critical current densities, the vortex phase diagram, and the effect of granularity of the stoichiometric high-Tc superconductor $CaKFe_4As_4$. *Phys. Rev. Mater.* **2018**, *2*, No. 074802.
(17) Todorov, I.; Chung, D. Y.; Claus, H.; Malliakas, C. D.; Douvalis, A. P.; Bakas, T.; He, J.; Dravid, V. P.; Kanatzidis, M. G. Topotactic redox chemistry of NaFeAs in Water and Air and superconducting behavior with stoichiometry change. *Chem. Mater.* **2010**, *22*, 3916−3925.
(18) Friederichs, G. M.; Schellenberg, I.; Pöttgen, R.; Duppel, V.; Kienle, L.; auf der Günne, J. S.; Johrendt, D. Metastable 11 K Superconductor $Na_{1-y}Fe_{2-x}As_2$. *Inorg. Chem.* **2012**, *51*, 8161−8167.
(19) Gooch, M.; Lv, B.; Sasmal, K.; Tapp, J. H.; Tang, Z. J.; Guloy, A. M.; Lorenz, B.; Chu, C. W. Superconductivity in ternary iron pnictides: AFe_2As_2 (A = alkali metal) and LiFeAs. *Phys. C* **2010**, *470*, 276−279.
(20) Zhou, X.; Wilfong, B.; Vivanco, H.; Paglione, J.; Brown, C. M.; Rodriguez, E. E. Metastable Layered Cobalt Chalcogenides from Topochemical Deintercalation. *J. Am. Chem. Soc.* **2016**, *138*, 16432−16442.
(21) Neilson, J. R.; McQueen, T. M. Bonding, Ion Mobility, and Rate-Limiting Steps in Deintercalation Reactions with $ThCr_2Si_2$-type KNi_2Se_2. *J. Am. Chem. Soc.* **2012**, *134*, 7750−7757.
(22) *ICSD − the Inorganic Crystal Structure Database*; FIZ − Karlsruhe, 2018.
(23) Ji, M.; Umemoto, K.; Wang, C. Z.; Ho, K. M.; Wentzcovitch, R. M. Ultrahigh-pressure phases of H_2O ice predicted using an adaptive genetic algorithm. *Phys. Rev. B* **2011**, *84*, No. 220105.
(24) Wu, S. Q.; Ji, M.; Wang, C. Z.; Nguyen, M. C.; Zhao, X.; Umemoto, K.; Wentzcovitch, R. M.; Ho, K. M. An adaptive genetic algorithm for crystal structure prediction. *J. Phys.: Condens. Matter.* **2014**, *26*, No. 035402.
(25) Zhao, X.; Nguyen, M. C.; Zhang, W. Y.; Wang, C. Z.; Kramer, M. J.; Sellmyer, D. J.; Li, X. Z.; Zhang, F.; Ke, L. Q.; Antropov, V. P.; Ho, K. M. Exploring the Structural Complexity of Intermetallic Compounds by an Adaptive Genetic Algorithm. *Phys. Rev. Lett.* **2014**, *112*, No. 045502.
(26) Gvozdetskyi, V.; Bhaskar, G.; Batuk, M.; Zhao, X.; Wang, R.; Carnahan, S. L.; Hanrahan, M. P.; Ribeiro, R. A.; Canfield, P. C.; Rossini, A. J.; Wang, C. Z.; Ho, K. M.; Hadermann, J.; Zaikina, J. V. Computationally-driven discovery of a family of layered LiNiB polymorphs. *Angew. Chem., Int. Ed.* **2019**, *58*, 15855−15862.
(27) *PDXL: Integrated X-ray powder diffraction software, Version 2.8.1.1*; Rigaku, 2018.
(28) Apex3, Version 2017.3, Bruker, USA.
(29) Sheldrick, G. M. A short history of SHELX. *Acta Crystallogr. A.* **2008**, *A64*, 112−122.
(30) Momma, K.; Izumi, F. VESTA 3 for three-dimensional visualization of crystal, volumetric and morphology data. *J. Appl. Crystallogr.* **2011**, *44*, 1272−1276.
(31) Chupas, P. J.; Chapman, K. W.; Kurtz, C.; Hanson, J. C.; Lee, P. L.; Grey, C. P. A versatile sample-environment cell for non-ambient X-ray scattering experiments. *J. Appl. Crystallogr.* **2008**, *41*, 822−824.
(32) Toby, B. H.; Von Dreele, R. B. GSAS-II: the genesis of a modern open-source all purpose crystallography software package. *J. Appl. Crystallogr.* **2013**, *46*, 544−549.
(33) Kresse, G.; Furthmuller, J. Efficiency of ab-initio total energy calculations for metals and semiconductors using a plane-wave basis set. *Comput. Mater. Sci.* **1996**, *6*, 15−50.
(34) Kresse, G.; Furthmuller, J. Efficient iterative schemes for ab initio total-energy calculations using a plane-wave basis set. *Phys. Rev. B* **1996**, *54*, 11169−11186.
(35) Kresse, G.; Joubert, D. From ultrasoft pseudopotentials to the projector augmented-wave method. *Phys. Rev. B* **1999**, *59*, 1758−1775.
(36) Bloechl, P. E. Projector augmented-wave method. *Phys. Rev. B* **1994**, *50*, 17953−17979.
(37) Perdew, J. P.; Burke, K.; Ernzerhof, M. Generalized Gradient Approximation Made Simple. *Phys. Rev. Lett.* **1996**, *77*, 3865−3868.
(38) Monkhorst, H. J.; Pack, J. D. Special points for Brillouin-zone integrations. *Phys. Rev. B* **1976**, *13*, 5188−5192.
(39) Chen, T. Contribution to the equilibrium phase diagram of the Mn−Bi system near MnBi. *J. Appl. Phys.* **1974**, *45*, 2358−2360.
(40) Gvozdetskyi, V.; Owens-Baird, B.; Hong, S.; Zaikina, J. V. Thermal stability and thermoelectric properties of NaZnSb. *Materials* **2018**, *12*, 48.
(41) Beleanu, A.; Kiss, J.; Kreiner, G.; Köhler, C.; Müchler, L.; Schnelle, W.; Burkhardt, U.; Chadov, S.; Medvediev, S.; Ebke, D.; Felser, C.; Cordier, G.; Albert, B.; Hoser, A.; Bernardi, F.; Larkin, T. I.; Pröpper, D.; Boris, A. V.; Keimer, B. Large resistivity change and phase transition in the antiferromagnetic semiconductors LiMnAs and LaOMnAs. *Phys. Rev. B* **2013**, *88*, No. 184429.
(42) Cui, J.; Kramer, M.; Zhou, L.; Liu, F.; Gabay, A.; Hadjipanayis, G.; Balasubramanian, B.; Sellmyer, D. Current progress and future challenges in rare-earth-free permanent magnets. *Acta Mater.* **2018**, *158*, 118−137.
(43) Honda, K. Die thermomagnetischen Eigenschaften der Elemente. *Ann. Phys.* **1910**, *337*, 1027−1063.
(44) Owen, M. Magnetochemische Untersuchungen. Die thermomagnetischen Eigenschaften der Elemente. II. *Ann. Phys.* **1912**, *342*, 657−699.
(45) McGuire, M. A.; Cao, H.; Chakoumakos, B. C.; Sales, B. C. Symmetry-lowering lattice distortion at the spin reorientation in MnBi single crystals. *Phys. Rev. B* **2014**, *90*, No. 174425.
(46) Lamichhane, T. N.; Rana, K.; Lin, Q.; Bud'ko, S. L.; Furukawa, Y.; Canfield, P. C. Near room temperature antiferromagnetic ordering with a potential low-dimensional magnetism in $AlMn_2B_2$. *Phys. Rev. Mater.* **2019**, *3*, No. 064415.
(47) Beeman, D.; Pincus, P. Nuclear Spin-Lattice Relaxation in Magnetic Insulators. *Phys. Rev.* **1968**, *166*, 359.
(48) Andresen, A. F.; Halg, W.; Fischer, P.; Stoll, E. The magnetic and crystallographic properties of MnBi studied by neutron diffraction. *Acta Chem. Scand.* **1967**, *21*, 1543−1554.
(49) Sarkar, A.; Mallick, A. B. Synthesizing the hard magnetic low-temperature phase of MnBi alloy: challenges and prospects. *JOM* **2020**, *72*, 2812−2825.
(50) Yang, J.; Yang, W.; Shao, Z.; Liang, D.; Zhao, H.; Xia, Y.; Yang, Y. Mn-based permanent magnets. *Chin. Phys. B* **2018**, *27*, No. 117503.
(51) Yoshida, H.; Shina, T.; Takahashi, T.; Fujimori, H. Preparation of highly pure MnBi intermetallic compounds by arc melting. *Mater. Trans.* **1999**, *40*, 455−458.
(52) Guo, X.; Chen, X.; Altounian, Z.; Strom-Olsen, J. O. Magnetic properties of MnBi prepared by rapid solidification. *Phys. Rev. B* **1992**, *46*, 14578−14582.
(53) Sharma, S. K.; Prakash, H. R.; Ram, S. Magnetic properties in MnBi alloy of small crystallites for permanent magnet devices. *AIP Conf. Proc.* **2016**, *1728*, No. 020657.
(54) Chen, Y.-C.; Sawatzki, S.; Ener, S.; Sepehri-Amin, H.; Leineweber, A.; Gregori, G.; Qu, F.; Muralidhar, S.; Ohkubo, T.; Hono, K.; Gutfleisch, O.; Kronmüller, H.; Schütz, G.; Goering, E. On the synthesis and microstructure analysis of high performance MnBi. *AIP Adv.* **2016**, *6*, No. 125301.

https://doi.org/10.1021/acs.chemmater.3c00140
Chem. Mater. 2023, 35, 3236−3248

(55) Kirkeminde, A.; Shen, J.; Gong, M.; Cui, J.; Rendevices, S. Metal-Redox Synthesis of MnBi Hard Magnetic Nanoparticles. *Chem. Mater.* **2015**, *27*, 4677−4681.
(56) Nguyen, V. V.; Poudyal, N.; Liu, X.; Liu, J. P.; Sun, K.; Kramer, M. J.; Cui, J. High-performance MnBi alloy prepared using profiled heat treatment. *IEEE Trans. Magn.* **2014**, *50*, 2105506.
(57) Cui, J.; Choi, J.-P.; Polikarpov, E.; Bowden, M. E.; Xie, W.; Li, G.; Nie, Z.; Zarkevich, N.; Kramer, M. J.; Johnson, D. Effect of composition and heat treatment on MnBi magnetic materials. *Acta Mater.* **2014**, *79*, 374−381.
(58) Williams, T. J.; Taylor, A. E.; Christianson, A. D.; Hahn, S. E.; Fishman, R. S.; Parker, D. S.; McGuire, M. A.; Sales, B. C.; Lumsden, M. D. Extended magnetic exchange interactions in the high-temperature ferromagnet MnBi. *Appl. Phys. Lett.* **2016**, *108*, No. 192403.
(59) Taufour, V.; Thimmaiah, S.; March, S.; Saunders, S.; Sun, K.; Lamichhane, T. N.; Kramer, M. J.; Bud'ko, S. L.; Canfield, P. C. Structural and Ferromagnetic Properties of an Orthorhombic Phase of MnBi Stabilized with Rh Additions. *Phys. Rev. Appl.* **2015**, *4*, No. 014021.

https://doi.org/10.1021/acs.chemmater.3c00140
Chem. Mater. 2023, 35, 3236−3248